How to cite: *Angew. Chem. Int. Ed.* **2023**, *62*, e202312936
doi.org/10.1002/anie.202312936

Molecular Qubits

A Heterometallic Porphyrin Dimer as a Potential Quantum Gate: Magneto-Structural Correlations and Spin Coherence Properties

Davide Ranieri, Alberto Privitera, Fabio Santanni, Karolina Urbanska, Grant J. Strachan, Brendan Twamley, Enrico Salvadori, Yu-Kai Liao, Mario Chiesa, Mathias O. Senge, Federico Totti, Lorenzo Sorace,* and Roberta Sessoli**

Abstract: In the development of two-qubit quantum gates, precise control over the intramolecular spin-spin interaction between molecular spin units plays a pivotal role. A weak but measurable exchange coupling is especially important for achieving selective spin addressability that allows controlled manipulation of the computational basis states $|00\rangle$ $|01\rangle$ $|10\rangle$ $|11\rangle$ by microwave pulses. Here, we report the synthesis and Electron Paramagnetic Resonance (EPR) study of a heterometallic meso-meso (m-m) singly-linked $V^{IV}O$–Cu^{II} porphyrin dimer. X-band continuous wave EPR measurements in frozen solutions suggest a ferromagnetic exchange coupling of ca. $8\cdot10^{-3}$ cm^{-1}. This estimation is supported by Density Functional Theory calculations, which also allow disentangling the ferro- and antiferromagnetic contributions to the exchange. Pulsed EPR experiments show that the dimer maintains relaxation times similar to the monometallic Cu^{II} porphyrins. The addressability of the two individual spins is made possible by the different **g**-tensors of V^{IV} and Cu^{II}-ions, in contrast to homometallic dimers where tilting of the porphyrin planes plays a key role. Therefore, single-spin addressability in the heterometallic dimer can be maintained even with small tilting angles, as expected when deposited on surface, unlocking the full potential of molecular quantum gates for practical applications.

Introduction

The electronic spin is an appealing candidate for the physical realization of qubits, the core units of the quantum computer.[1] It has an intrinsic quantum nature and can be coherently manipulated with microwave radiation, as commonly done in pulsed electron paramagnetic resonance (EPR).[2] Even if most efforts have been devoted to spin impurities in semiconductors and inorganic lattices,[3,4] molecular spins are an attractive alternative because of their chemical versatility and ease of processing.[5–7] Molecules are also ideal candidates for realizing multiple qubits and quantum logic gates.[6,8] A controlled-NOT (C-NOT) two-qubit gate is indeed sufficient, in combination with single qubit gates, to form a universal set for quantum computation.[9] The four necessary computational basis states, namely $|00\rangle$ $|01\rangle$ $|10\rangle$ $|11\rangle$, can be realized with two spins $^1/_2$ as in a bimetallic paramagnetic complex. On one hand, the two spins must be appropriately coupled to differentiate the energy gaps and, thus, the excitation frequency of each transition inside the four-level space. On the other hand, too strong exchange interactions do not allow single-spin addressability, which requires that the two coupled spins are distinguishable.[6,8] The electron spins can either be different in nature, e.g., having different true or effective *g* values,[10,11] or they can be identical but with their anisotropic magnetic tensors oriented differently in space.[12] Considering the other fundamental requirement, i.e., the long lifetime of the coherence of any superposition state,[9]

[*] D. Ranieri, Dr. A. Privitera, Dr. F. Santanni, Prof. Dr. F. Totti, Prof. Dr. L. Sorace, Prof. Dr. R. Sessoli
Department of Chemistry "Ugo Schiff" & INSTM RU, University of Florence
Via della Lastruccia 3, 50019 Sesto Fiorentino (Italy)
E-mail: lorenzo.sorace@unifi.it
roberta.sessoli@unifi.it

Dr. A. Privitera
Department of Industrial Engineering & INSTM RU, University of Florence
Via Santa Marta 3, 50139 Firenze (Italy)

Dr. K. Urbanska, Dr. G. J. Strachan, Prof. Dr. M. O. Senge
School of Chemistry, Chair of Organic Chemistry, Trinity Biomedical Sciences Institute, Trinity College Dublin, The University of Dublin, 152-160 Pearse Street, D02R590 Dublin (Ireland)
E-mail: sengem@tcd.ie

Dr. B. Twamley
School of Chemistry, Trinity College Dublin, The University of Dublin, Dublin 2 (Ireland)

Prof. Dr. E. Salvadori, Dr. Y.-K. Liao, Prof. Dr. M. Chiesa
Department of Chemistry and NIS, University of Turin,
Via P. Giuria 7, 10125 Torino (Italy)

Prof. Dr. M. O. Senge
Institute for Advanced Study (TUM-IAS), Technical University of Munich, Focus Group—Molecular and Interfacial Engineering of Organic Nano-systems
Lichtenberg-Str.2a, 85748 Garching (Germany)

3d metal ions are very appealing. Record coherence times have been obtained for vanadium(IV) ions (V^{IV}) with nuclear spin-free ligands, while coherence persists up to room temperature in copper(II) (Cu^{II}) and V^{IV} complexes. An interesting example of spectral addressability and long relaxation times is a Cu^{II} porphyrin complex functionalized with a carboxylate group coordinating a $[Ti^{III}Cp_2]^+$ unit.[11]

Multi-porphyrin systems offer the advantage of superior chemical stability compared to ligands hitherto used to develop molecular quantum gates. When neutral, they can be deposited by sublimation on various surfaces,[13–15] making their embedding in devices more feasible. In addition, surface-induced reactivity has been exploited to produce flat triply-linked porphyrin nano tapes.[16–18] Studies on the exchange-coupling in porphyrin metal dimers evidenced moderate antiferromagnetic interactions promoted by the conjugation in doubly- and triply-linked porphyrins,[19–23] while meso-meso singly-linked homometallic Cu^{II} dimers exhibit negligible exchange interactions.[19] We recently demonstrated that the vanadyl analog shows a measurable exchange interaction of the order of $10^{-2}\,cm^{-1}$.[23] Interestingly, due to the tilting of the two porphyrin planes and the anisotropy of the vanadyl ***g***- and ***A***- tensors, the two spin centers in this complex are distinguishable in almost all orientations of the external magnetic field. In addition, the good coherence properties of the monomeric units are retained in the dimer, a finding that has been recently generalized to vanadyl dimers coupled through a delocalized π-system.[22] The increased exchange coupling in the vanadyl complex was justified by the fact that the vanadyl magnetic orbital lies slightly above the porphyrin plane. The saddle-like distortion of the porphyrin ring,[24] when coordinated to the $V^{IV}O$ unit, further induces the mixing of the in-plane porphyrin orbitals with the out-of-plane ones.

Here, we investigated whether the key role of the vanadyl unit in promoting a significant magnetic exchange interaction is maintained even when coupled to a different paramagnetic center in a heterometallic $V^{IV}O$–Cu^{II} bisporphyrin using H_2DPP (5,15-diphenylporphyrin). This porphyrin ligand was selected as a compromise between solubility and decoherence induced by hydrogen magnetic nuclei on the ligand and is also suited for thermal sublimation experiments. Moreover, this choice also represents a good building block for extended arrays of porphyrin rings. Additionally, we focused on singly-linked porphyrin to avoid the stronger coupling promoted by triply linked porphyrins.[19] We found that the exchange interaction, though weaker than in the homometallic vanadyl dimer, clearly impacts the EPR spectrum, causing a sizeable splitting of the resonance lines. The difference in the *g*-factors of the two metal centers suggests that individual spin addressability will also be retained when depositing the dimer on a surface, where flattening of the molecules is expected.[25]

Results and Discussion

Retrosynthetically, the synthesis of unsymmetric m-m and/or β-β directly-linked bisporphyrins requires a stepwise approach, ideally using precursors with two different but complementary functional groups.[26] This was exemplified in *Osuka* and co-workers' synthesis of hybrid porphyrins, e.g., heterobimetallic Ni^{II}-Zn^{II} and free base-Zn^{II} hybrids.[27,28]

Following this strategy, the monomeric porphyrin complexes (Scheme 1) were synthesized by reacting H_2DPP with $VO(acac)_2$[29] or $Cu(AcO)_2$[30] to yield the respective metalloporphyrin **1** or **2** (Scheme 1, A). The oxidative coupling step employing brominated porphyrins in the dimerization procedure[31] did not yield the dimer and therefore we used iodinated derivatives obtained by following published procedures.[31,32] Monomer **1** was used to obtain the iodinated derivative **3**, while the free base H_2DPP was first iodinated, to yield 5-iodo-10,20-diphenylporphyrin (H_2IDPP) and subsequently metalated with $Cu(OAc)_2$ to obtain monomer **4** (Scheme 1, A). The yield of the iodination did not change significantly upon using various oxidative agents such as $CuCl_2$, PIFA ((bis(trifluoroacetoxy)iodo)benzene), or $AgPF_6$. PIFA was then chosen as the oxidizing agent to reduce metal contamination of the final products, which were purified by column chromatography. The borylated compound **5** (Scheme 1, B) was synthesized according to a literature procedure.[31] The synthesis of compounds **3**, **4**, and **5**, allowed an entry into the hybrid porphyrin dimers. For the synthesis of the hybrid dimers **6** and **7**, a *Suzuki–Miyaura* coupling[33] was performed between the pinacolborane **5** and iodinated porphyrins **3** or **4** (Scheme 1, B).[34,35] Finally, the

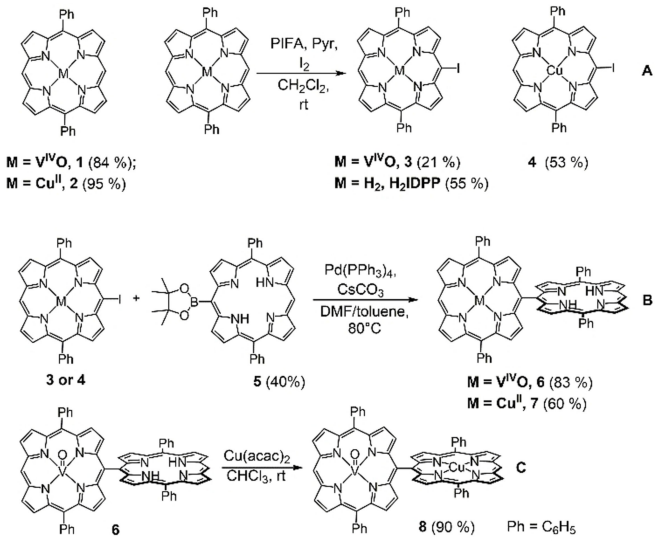

Scheme 1. (A) Chemical structures of the synthesized monomeric porphyrins, along with the iodination reaction. (B) Scheme of the reaction of the iodinated $V^{IV}O$ (**3**) or Cu^{II} (**4**) porphyrin with the borylated porphyrin **5** to obtain hybrid porphyrin dimers **6** or **7**. (C) The free base porphyrin unit in **6** is metalated with $Cu(acac)_2$ to yield the heterometallic porphyrin dimer **8**. Experimental yields are given in parentheses.

metalation of the free base porphyrin unit in compound **6** with $Cu(acac)_2$ in $CHCl_3$ at room temperature afforded compound **8** (Scheme 1, C). To obtain **8**, metalation of **6** was preferred over that of **7** due to the milder reaction conditions required for the former. Detailed synthetic procedures and chemical characterization for all molecules prepared in this work can be found in the Supporting Information (Section S1, Figures S1–S8).

Purple single crystals of monomers **1** and **2** were obtained by slow evaporation of a CH_2Cl_2/MeCN (10:1) mixture and a $CHCl_3$/heptane (7:1) mixture, respectively. Both compounds crystallized in the monoclinic space group $P2_1/c$ (see Table S1 for details of crystallographic data collections). For **1**, the asymmetric unit is half of the molecule, the V=O group being disordered over inversion above and below the porphyrin plane (Figure S9).[36] For **2**, the asymmetric unit includes the porphyrin unit with one $CHCl_3$ molecule of solvation (Figure S9). The porphyrin plane in compound **2** exhibits out-of-plane ruffled distortion.

Crystallization of the dimers **6–8** was hampered by their low solubility in toluene and ethers and only limited solubility in $CHCl_3$ or CH_2Cl_2. This resulted in fast precipitation during the slow evaporation process, thus limiting the sizes of the crystals obtained and the quality of the data collection. However, the basic features of the molecular structures were obtained, providing crucial information on the chemical identity, connectivity of the complexes, and on the tilting angle between the two moieties. A detailed discussion on disorder modeling is reported in Section S2. In the case of compound **7**, attempts to get single crystals were unsuccessful.

Compound **6** crystallized in the tetragonal space group P4cc (n. 103), and the refined structure evidences a high degree of disorder (see Figure S10). The asymmetric unit consists of one porphyrin moiety with 50 % metal occupancy, the dimer showing a C_2-axis perpendicular to the meso-meso bond. The resulting tilt angle between the porphyrin planes θ, defined as the dihedral angle about the meso-meso bond, is 78°, close to that observed in a homometallic $V^{IV}O$-dimer;[23] a similar saddle-like distortion is also observed. The shortest intermolecular VO–VO distance is around 8.5 Å. The structure shows solvent-accessible voids occupying 4.1 % of the unit cell volume, which are visible along the *c* axis (Figure S11). Compound **8** crystallizes in the tetragonal space group P4/ncc (n.130). The asymmetric unit is half a porphyrin unit, with partial $V^{IV}O$ and Cu^{II} occupancy, and the former being disordered above and below the porphyrin plane. A C_2-axis passing through the meso carbon atoms and an S_4-axis bisecting the meso-meso bond generates the dimeric unit. The tilting angle θ between porphyrin planes is around 78° (Figure 1b) and the intramolecular V–Cu distance is around 8.4 Å, which compares well with the 8.37 Å observed in the homometallic vanadyl dimer.[23] Despite the low quality of the crystal structure, the simulated Powder X-Ray Diffraction pattern compares well with the experimental one (see Figure S12).

X-band continuous wave (cw) EPR measurements were carried out to gain insight into the magnetic interactions in compounds **1**, **2**, **6**, **7**, and **8**. All spectra were recorded in a

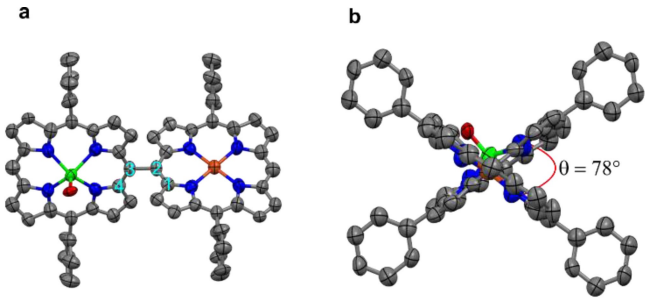

Figure 1. (**a**) Molecular structure of compound **8** in the crystal. (**b**) Molecular structure of compound **8** viewed along the meso-meso linkage. The angle θ, describing the tilting between the porphyrin units, is defined as the dihedral angle between the carbon atoms 1–4 labeled in **a**.

frozen solution of a 0.2 mM 1:1 toluene/CH_2Cl_2 mixture at 30 K. The experimental and simulated spectra of the monomers **1** and **2** and their monometallic dimers **6** and **7** are shown in the Supporting Information (Figures S13 and S14) and Figure 2 (left, turquoise and red lines). The simulations of the monometallic porphyrins were performed based on the spin-Hamiltonian:[37]

$$\hat{H}_M = \mu_B \vec{B} \cdot \boldsymbol{g}_M \cdot \hat{\boldsymbol{S}}_M + \hat{\boldsymbol{S}}_M \cdot \boldsymbol{A}_M \cdot \hat{\boldsymbol{I}}_M + \sum_{i=1}^{4} \hat{\boldsymbol{S}}_M \cdot \boldsymbol{A}_N \cdot \hat{\boldsymbol{I}}_{N,i} \qquad (1)$$

where $\boldsymbol{g}_M$ is the $\boldsymbol{g}$-tensor of the metal porphyrin, and $\boldsymbol{A}_M$ and $\boldsymbol{A}_N$ are the hyperfine coupling tensors for the metal and the pyrrolic nitrogen nuclei. In our simulations we assumed a local electronic C_{4v} symmetry, $\boldsymbol{g}_M$ and $\boldsymbol{A}_M$ tensors being collinear and axial.

The spectrum of **6** in Figure 2 (left), as that of **1** in Figure S13, shows the characteristic EPR powder pattern of vanadyl porphyrins due to the anisotropic hyperfine coupling of the electron spin with the ^{51}V ($I=7/2$) nucleus. No sign of coupling with the four nearby nitrogen atoms of the porphyrin unit is observed since the d_{xy} magnetic orbital of the vanadyl ion is not pointing directly toward the nitrogen donors. The last term of the Hamiltonian (1) can therefore be neglected. Similarly, the spectra of **2** and **7** (see Figure 2 and S14) show the typical pattern of Cu^{II} porphyrins due to the anisotropic hyperfine interaction of the electron spin with nuclei of Cu (^{63}Cu, natural abundance, NA = 69.17 %; ^{65}Cu, NA = 30.83 %; both $I=3/2$) and the four coordinated ^{14}N ($I=1$). The simulation parameters for all the monometallic porphyrins (Table 1) agree with values in the literature.[29,38,39] Notably, the simulation values of the monometallic dyads **6** and **7** are very similar to their monomeric counterparts **1** and **2**. This highlights that even after the introduction of an additional porphyrin unit, both $\boldsymbol{A}_M$ and $\boldsymbol{g}_M$ tensors remain axial within the spectral resolution of X-band cw-EPR spectroscopy.

The EPR spectrum of compound **8** (Figure 2 left, black line, other spectra available as Figure S15–S16) differs from the superposition of the spectra of the two metal ions. It is also characterized by a larger linewidth than the monome-

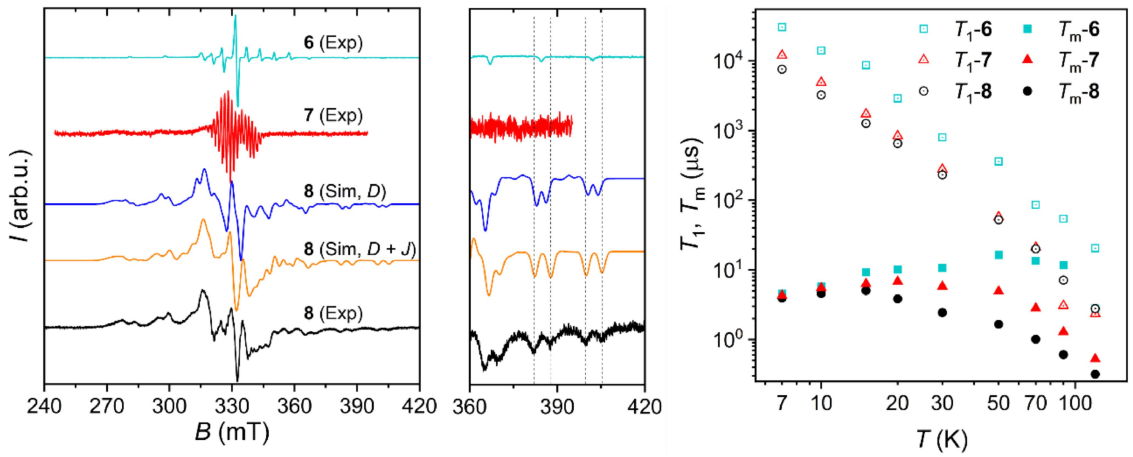

Figure 2. Left: Experimental X-band cw-EPR spectra ($T=30$ K, frozen solution 0.2 mM in 1:1 toluene/CH_2Cl_2) of the compounds **6** ($\nu=9.392$ GHz, magenta line), **7** ($\nu=9.402$ GHz, brown line), and **8** ($\nu=9.394$ GHz, black line) together with two relevant spectral simulations of compound **8**. The reported simulations were performed at two different values of J (0 and $-8.0\cdot10^{-3}$ cm^{-1}) by keeping the dipolar interaction and $\theta=78°$ constant to highlight the effect of the exchange interaction. Middle: magnification of the high fields spectral region to appreciate the impact of the exchange interaction. The parameters of the simulations are reported in Table 1. Right: Temperature dependence of T_1 (dotted symbols) and T_m (solid symbols) for compounds **6** (turquoise squares), **7** (red triangles), and **8** (black circles) measured at 340 mT at X-band frequency in a 0.2 mM d_8-toluene frozen solution.

Table 1: Principal values of the Spin-Hamiltonian tensors for compounds **1**, **2**, **6**, **7**, and **8** and isotropic exchange coupling constant obtained from the simulation of frozen solution samples. For the simulation of the spectra of **8**, a tilting angle of 78° was assumed between Cu^{II} and V^{IV} tensors. ***D*** has been calculated in the point-dipole approximation with z perpendicular to the Cu-porphyrin plane and y along the meso-meso bond.

	1, 2, 8		6, 7, 8			8	
	g_V	A_V (MHz)	g_{Cu}	A_{Cu} (MHz)	A_N (MHz)	D (cm^{-1})	J (cm^{-1})
x	1.985	162	1.985	60	54	$3.0\cdot10^{-3}$	
y	1.985	162	1.985	60	43	$-6.2\cdot10^{-3}$	$-8\cdot10^{-3}$
z	1.964	475	1.964	626	45	$3.2\cdot10^{-3}$	

tallic dimers, most likely attributable to the dipolar coupling interaction between the two unpaired electron spins of the dyad and a possible distribution of dihedral angles between the two porphyrin units in the frozen solution. The EPR spectrum was simulated using the following Spin-Hamiltonian:

$$\hat{\boldsymbol{H}}_{V-Cu} = \mu_B\vec{\boldsymbol{B}}\cdot\boldsymbol{g}_V\cdot\hat{\boldsymbol{S}}_{VO} + \hat{\boldsymbol{S}}_{VO}\cdot\boldsymbol{A}_V\cdot\hat{\boldsymbol{I}}_V + \mu_B\vec{\boldsymbol{B}}\cdot\boldsymbol{g}_{Cu}\cdot\hat{\boldsymbol{S}}_{Cu} + \hat{\boldsymbol{S}}_{Cu}\cdot\boldsymbol{A}_{Cu}\cdot\hat{\boldsymbol{I}}_{Cu} + \sum_{i=1}^{4}\hat{\boldsymbol{S}}_{Cu}\cdot\boldsymbol{A}_{N,i}\cdot\hat{\boldsymbol{I}}_N + \hat{\boldsymbol{S}}_{VO}\cdot\boldsymbol{J}_{V-Cu}\cdot\hat{\boldsymbol{S}}_{Cu} \quad (2)$$

that adds to the Zeeman and hyperfine interaction terms of the single centers the interaction contribution described by the matrix $\boldsymbol{J}_{V-Cu}$. The latter comprises the isotropic component of the exchange interaction J and the through-space dipolar coupling ***D***, while we neglected the antisymmetric term:[40]

$$\boldsymbol{J}_{V-Cu} \approx J\boldsymbol{I} + \boldsymbol{D} = \begin{bmatrix} J+D_X & 0 & 0 \\ 0 & J+D_Y & 0 \\ 0 & 0 & J+D_Z \end{bmatrix} \quad (3)$$

To reduce the number of free parameters, the $\boldsymbol{g}_M$ and ***A*** tensors principal values were fixed at those of their respective monometallic dimers, and their local z axis assumed to be perpendicular to the porphyrin planes. Further, the tilting angle between the two porphyrin units was fixed at the experimental value of $\theta=78°$, and ***D*** was calculated in the point-dipole approximation using the X-ray data and relative ***g***-tensor orientations.[23] We note that, due to the relatively small g-anisotropy, the calculated ***D*** tensor is essentially axial, with the main axis being directed along the V–Cu direction. Thus, it is not affected by variation of the dihedral angle.[40] Consequently, the only variable parameter was the exchange interaction J. The splitting of the outermost lines, corresponding to the parallel transitions of the $V^{IV}O$ unit, provides a first clue as to the magnitude of the exchange interaction. The splitting simulated by assuming a purely dipolar coupling (i.e., fixing $J=0$) is clearly smaller than that observed in the experiment. A preliminary survey (Figure S17) indicates that the correct splitting of those lines can be obtained with either $J=2\cdot10^{-3}$ (antiferromagnetic, AF) or $J=-8\cdot10^{-3}$ cm^{-1} (ferromagnetic, FM). The reason for this difference is that in the direction of V=O bond (i.e., the direction of those EPR transitions) the dipolar interaction is AF. FM exchange interactions larger than AF ones are therefore necessary to obtain the same splitting, which is proportional to $|J+D_z|$. The survey further shows that the central part of the spectrum is much better reproduced using $J=-8\cdot10^{-3}$ cm^{-1} than $J=+2\cdot10^{-3}$ cm^{-1}. This is also the case for the simulation of

pseudomodulated Q-band spectrum (Figure S18). Notably, in contrast to the homometallic vanadyl dimer,[23] the simulated spectra of the heterometallic dimer **8** do not change significantly with the g_M and A_M- tensors tilting angle, as shown in Figure S19.

The EPR data clearly show that the VO–Cu exchange coupling is weakly FM (the best simulation is reported in Figure 2 and corresponding parameters in Table 1). Its magnitude falls between those reported for structurally similar meso-meso linked Cu–Cu[19] and VO–VO[23] homometallic dimers, albeit being of opposite sign.

This confirms our prediction, based on the deformations brought in by $V^{IV}O$ coordination, that local σ (in-plane) and delocalized π (out-of-plane) contributions are responsible for the super-exchange interaction.[23] A comparison between the UV/Vis spectra of VO–Cu and VO–VO dimers (Figure S1) confirms the higher conjugation in the latter, which shows larger line broadening and more red-shifted Q-bands.[41,42]

The spin relaxation properties of compounds **6**–**8** were studied by pulsed EPR spectroscopy at X-band frequency. Temperature-dependent inversion recovery and primary echo decay experiments were used to determine the longitudinal (T_1) and transverse (T_m) relaxation times in the interval between 7 and 120 K. The samples were dissolved in d_8-toluene (0.2 mM) and measured as frozen solutions. All measurements were performed at a magnetic field setting corresponding to the maximum intensity of echo detected EPR spectrum (Figure S20). T_m values were extracted by fitting the experimental decay traces using a stretched exponential function, while T_1 values were obtained by a biexponential fitting of the inversion recovery traces (Figure S21–S23 and Table S2). In Figure 2, only the slow component of the biexponential fit, usually taken to represent the spin-lattice relaxation (T_1), is plotted; the fast component[43,44] is associated with spectral diffusion effects[43,44] (i.e., excitation bandwidth smaller than the spectral width) and, thus, is not shown.

Compound **6** has T_1 and T_m values longer than compound **7**. In both cases, these values are comparable with the relaxation times of other monomeric $V^{IV}O$[29,45,46] or Cu^{II} complexes.[46–48] The faster spin-lattice relaxation of Cu^{II} can be attributed to the larger spin-orbit coupling that makes the spin system more sensitive to molecular vibrations. Compound **8** has T_1 values very similar to **7**, suggesting that the presence of the nearby slower relaxing vanadyl unit does not negatively impact the spin-lattice relaxation. T_m values of **8** are instead slightly faster than those of **6** and **7** and also lower than those reported for dimeric $V^{IV}O$ bimetallic complexes, including the homometallic vanadyl porphyrin dimer.[11,22,49,50]

The accurate determination of the Spin-Hamiltonian parameters of **8** allows us to envision the microwave operation of the dimeric unit as a C-NOT quantum gate. This is fundamental for realizing a universal quantum computer. We define the computation states by choosing the V and Cu electronic spins as control and target qubits, respectively (Figure 3a). By applying a field of 1.3 T, the nuclear and electronic spin states are factorized, and the

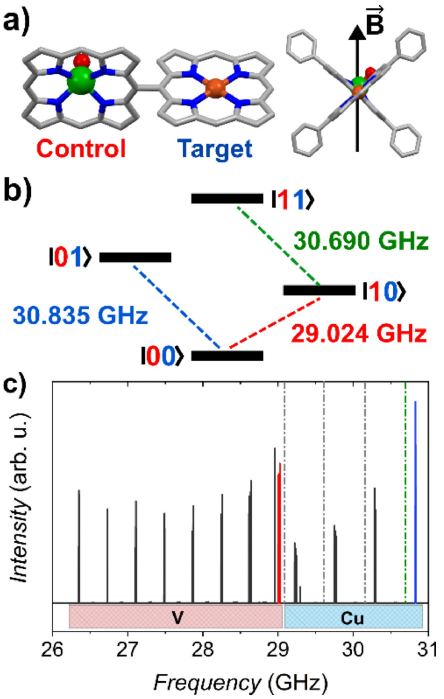

Figure 3. a) Orientation of the static magnetic field with respect to the control and target qubits; b) Computed energy differences between states involving control (red) and target qubit (blue and green) electronic spin transitions highlighted with the same color in the frequency-swept absorption spectrum (c) simulated for $B = 1.3$ T, $T = 100$ mK and the Spin-Hamiltonian parameters reported in Table 1. Gray dashed lines refer to other possible choices of hyperfine levels of the target.

microwave radiation in the Q-band range (ca. 30 GHz) induces transition from the $m_s = -1/2$ to the $m_s = +1/2$ states (labelled as computational states $|0\rangle$ and $|1\rangle$ in Figure 3b).

In difference to the homometallic vanadyl dimer, addressability of the two spins in **8** is warranted for most orientations of the static magnetic field, including along the bisector of the two porphyrin planes. Figure 3c shows the frequency-swept absorption spectrum computed for this orientation at 100 mK (see Figure S24 for simulation at 10 K). The spectrum can be divided into a low-frequency region where the eight hyperfine transitions of the ^{51}V are visible and a high-frequency region where four transitions (shown only for the ^{65}Cu isotope for clarity) can be identified. The nuclear spins are not polarized at this temperature and the intensity is almost equally distributed over the different hyperfine lines. Focusing on the highest hyperfine transition of the target qubit, we compute that the transition occurs at 30.835 GHz if the control qubit is in its ground state ($|00\rangle \rightarrow |01\rangle$, blue line in Figure 3b and 3c). Upon excitation of the control qubit—for instance irradiating at 29.024 GHz (red line)—absorption of microwaves at 30.690 GHz occurs, corresponding to the $|10\rangle \rightarrow |11\rangle$ transition (green line). Different hyperfine lines of the target can be selected to reduce the frequency separation between the control and the target absorptions, while maintaining ca. 200 MHz of separation induced by the control (gray dashed

lines in Figure 3c), as commercial low-Q cavities have a bandwidth of ca. 400 MHz.

Interestingly, the scenario described in Figure 3 is rather robust against different operating conditions. If the static magnetic field is aligned along the target z axis, the target and control transitions are slightly more separated in frequency (see Figure S25–S26), while a separation similar to that in Figure 3c is observed upon reduction of the tilting angle between the two porphyrin units (see Figure S27–S28).

Density Functional Theory (DFT) geometry optimization in gas-phase was carried out to shed light on the structural properties of compound **8** because of the low quality of the experimental structure determination. The results are reported in Figure S29 and some selected distances are given in Table S3. The tilting angle of the optimized structure, $\theta \approx 84°$, is close to the value $\theta \approx 78°$ of the X-ray structure. The corresponding calculated J value ($-1.2 \cdot 10^{-2}\,cm^{-1}$) is in very good agreement with the one estimated from the EPR simulations and confirms the trend expected upon substituting vanadyl with copper ions in singly-linked porphyrin dimers, i.e., a reduction in the magnitude of the coupling and a change of the nature of the coupling from AF to FM.[23]

This observation corresponds to the behavior of the seminal copper/vanadyl dimer reported by Kahn et al.,[51] but at a different level of complexity. The magnetic orbitals of the $Cu^{II}(d_{x^2-y^2})$ and $V^{IV}O$ (d_{xy}) ions are orthogonal by symmetry (see Figure 4), justifying the FM nature of the interaction in **8** and its smaller value in comparison to the homometallic $V^{IV}O$-dimer.[23] Moreover, as the Cu^{II} ion lies in the plane of the porphyrin ligand, the overlap of the magnetic orbital with the porphyrin out-of-plane orbitals (π-system) is minimal. This significantly reduces the antiferromagnetic contributions that are active when the porphyrin rings are tilted.

To analyze this point in more depth, we performed single-point J value calculations on two additional geometries. The first corresponds to the tilting angle set to the value determined by single crystal X-ray analysis, while the second represents a possible critical point where the tilting angle is set to 90°. No significant difference in J between the X-ray and optimized structures is computed, while a small reduction in the magnitude of J is derived for $\theta = 90°$ (see Table S4). The presence of two pathways, the FM one through σ porphyrin orbitals and the AF one involving π orbitals, nicely explains the different angular dependence of the computed exchange interaction in **8** compared to the homometallic $V^{IV}O$-dimer. For the latter, angles close to 90° correspond to a relative maximum of $|J|$. The exchange interaction mediated by out-of-porphyrin-plane orbitals is expected to be AF and maximum at $\theta = 90°$, where the overlap with the in-plane orbital of the metal unit is highest. In the case of the Cu–VO dimer, this AF contribution adds to the FM one with the opposite sign, thus slightly reducing $|J|$ for $\theta = 90°$.

We also computed the exchange coupling for an optimized structure of a triply-fused dimer (Figure S30 and S31). As expected, a much stronger FM coupling of $J = -0.36\,cm^{-1}$ is calculated, which would hamper the single spin addressability. Similar to the singly-linked case, the sign of the coupling is consistent with Kahn's model. Its magnitude is intermediate between triply-fused Cu[19] and VO homometallic dimers,[22] the former being the largest.

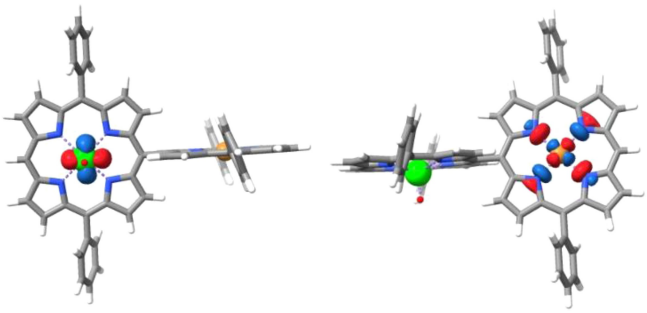

Figure 4. Two orthogonal views of the isodensity ($\psi = 0.05$ (e bohr^{-3})$^{1/2}$) surfaces of magnetic orbitals for compound **8** computed at the B3LYP level. The code color is V (green), Cu (orange), N (blue), O (red), C (gray), and H (white).

Conclusion

The combined results in this and our previous work[23] show that paramagnetic bimetallic $V^{IV}O$ bisporphyrins are promising candidates for developing two-qubit quantum gates. It is possible to obtain paramagnetic singly metalated bisporphyrins (compounds **6** and **7**) through a *Suzuki–Miyaura* coupling.[31,52] By metallating compound **6**, we obtained a paramagnetic and heterometallic porphyrin dimer in very good yields. We demonstrated by means of cw-EPR and DFT calculations that J is smaller than in the vanadyl homometallic dimer,[23] but still strong enough to be measured with a standard X-band cw-EPR spectrometer. With this set of parameters, single spin addressability, a fundamental prerequisite for the realization of a C-NOT quantum gate, is possible, in principle, over a wide range of experimental conditions.

Furthermore, both spectral simulations and DFT calculations revealed that the weak exchange interaction is ferromagnetic. The magnitude and sign of J are explained by the competitive in-plane and out-of-plane super-exchange pathways made possible by the pentacoordinate $V^{IV}O$ unit. Our study identifies the $V^{IV}O$ unit as a key ingredient to enhance the magnetic exchange interaction in oligo-porphyrin structures, and similar J values are expected in other heterometallic combinations containing $V^{IV}O$ porphyrins. Interestingly, the relaxation times T_m and T_1 of the dimer do not vary significantly from monomeric Cu^{II}[46–48] or $V^{IV}O$ porphyrins,[29,45,46] suggesting that the additional paramagnetic unit does not substantially affect decoherence. The combined exchange and coherence properties of this system form a sound starting point to investigate its single-molecule properties once deposited on surfaces.

Supporting Information

Additional details on the synthetic procedures, crystal structure determination, and EPR spectroscopy investigation. Further information on the DFT calculations and selected parameters of the optimized molecular structures. The authors have cited additional references within the Supporting Information..[53–70]

Acknowledgements

This work was supported by the European Union through the FETOPEN project FATMOLS (GA 862893) and by the NextGenerationEU funds through the Italian MUR National Recovery and Resilience Plan, Mission 4 Component 2—Investment 1.4—National Center for HPC, Big Data and Quantum Computing—CUP B83C22002830001), Investment 1.3 (PE0000023-NQSTI), and Investment 1.2—Project ID: SOE_0000064—PHOTOCODE (A. P.). The support of MUR through Progetto Dipartimenti di Eccellenza 2018–2022 (CUP B96 C1700020008) and 2023–2027 (CUP B97G22000740001—DICUS 2.0 for F. T., L. S., R. S. and CUP D13C22003520001—Project CH4.0 for E. S. and M. C.) is acknowledged. The work was supported by the Science Foundation Ireland (SFI award 21/FFP-A/9469) and the Irish Research Council (GOIPD/2021/479). The support of the Technical University of Munich—Institute for Advanced Study through a Hans Fischer Senior Fellowship (M. O. S.) is also acknowledged. We thank the Centro di Servizi di Spettrometria di Massa (CISM) of the University of Florence.

Conflict of Interest

The authors declare no conflict of interest.

Data Availability Statement

The data that support the findings of this study are available from the corresponding author upon reasonable request.

Keywords: DFT Calculations · EPR-Spectroscopy · Hybrid Porphyrin Dimers · Molecular Spin Qubits

[1] J. P. Dowling, G. J. Milburn, *Philos. Trans. R. Soc. A* **2003**, *361*, 1655–1674.
[2] G. Wolfowicz, J. J. L. Morton, *eMagRes* **2016**, *5*, 1515–1528.
[3] A. Chatterjee, P. Stevenson, S. De Franceschi, A. Morello, N. P. de Leon, F. Kuemmeth, *Nat. Rev. Phys.* **2021**, *3*, 157–177.
[4] L. M. K. Vandersypen, M. A. Eriksson, *Phys. Today* **2019**, *72*, 38–45.
[5] F. Luis, S. Hill, E. Coronado, *Nat. Chem.* **2019**, *11*, 301–309.
[6] M. Atzori, R. Sessoli, *J. Am. Chem. Soc.* **2019**, *141*, 11339–11352.
[7] M. R. Wasielewski, M. D. E. Forbes, N. L. Frank, K. Kowalski, G. D. Scholes, J. Yuen-Zhou, M. A. Baldo, D. E. Freedman, R. H. Goldsmith, T. Goodson, M. L. Kirk, J. K. McCusker, J. P. Ogilvie, D. A. Shultz, S. Stoll, K. B. Whaley, *Nat. Chem. Rev.* **2020**, *4*, 490–504.
[8] F. Troiani, M. Affronte, *Chem. Soc. Rev.* **2011**, *40*, 3119–3129.
[9] D. P. DiVincenzo, *Fortschr. Phys.* **2000**, *48*, 771–783.
[10] D. Aguilà, L. A. Barrios, V. Velasco, O. Roubeau, A. Repollés, P. J. Alonso, J. Sesé, S. J. Teat, F. Luis, G. Aromí, *J. Am. Chem. Soc.* **2014**, *136*, 14215–14222.
[11] S. Von Kugelgen, M. D. Krzyaniak, M. Gu, D. Puggioni, J. M. Rondinelli, M. R. Wasielewski, D. E. Freedman, *J. Am. Chem. Soc.* **2021**, *143*, 8069–8077.
[12] S. Nakazawa, S. Nishida, T. Ise, T. Yoshino, N. Mori, R. D. Rahimi, K. Sato, Y. Morita, K. Toyota, D. Shiomi, M. Kitagawa, H. Hara, P. Carl, P. Höfer, T. Takui, *Angew. Chem. Int. Ed.* **2012**, *51*, 9860–9864.
[13] I. Cimatti, L. Bondì, G. Serrano, L. Malavolti, B. Cortigiani, E. Velez-Fort, D. Betto, A. Ouerghi, N. B. Brookes, S. Loth, M. Mannini, F. Totti, R. Sessoli, *Nanoscale Horiz.* **2019**, *4*, 1202–1210.
[14] L. Malavolti, M. Mannini, P. E. Car, G. Campo, F. Pineider, R. Sessoli, *J. Mater. Chem. C* **2013**, *1*, 2935–2942.
[15] T. Lukasczyk, K. Flechtner, L. R. Merte, N. Jux, F. Maier, J. M. Gottfried, H. P. Steinrück, *J. Phys. Chem. C* **2007**, *111*, 3090–3098.
[16] Q. Sun, L. M. Mateo, R. Robles, N. Lorente, P. Ruffieux, G. Bottari, T. Torres, R. Fasel, *Angew. Chem. Int. Ed.* **2021**, *60*, 16208–16214.
[17] L. M. Mateo, Q. Sun, S. X. Liu, J. J. Bergkamp, K. Eimre, C. A. Pignedoli, P. Ruffieux, S. Decurtins, G. Bottari, R. Fasel, T. Torres, *Angew. Chem. Int. Ed.* **2020**, *59*, 1334–1339.
[18] L. M. Mateo, Q. Sun, K. Eimre, C. A. Pignedoli, T. Torres, R. Fasel, G. Bottari, *Chem. Sci.* **2021**, *12*, 247–252.
[19] N. Wili, S. Richert, B. Limburg, S. J. Clarke, H. L. Anderson, C. R. Timmel, G. Jeschke, *Phys. Chem. Chem. Phys.* **2019**, *21*, 11676–11688.
[20] Y. Inokuma, N. Ono, H. Uno, D. Y. Kim, S. B. Noh, D. Kim, A. Osuka, *Chem. Commun.* **2005**, 3782–3784.
[21] T. Ikeue, K. Furukawa, H. Hata, N. Aratani, H. Shinokubo, T. Kato, A. Osuka, *Angew. Chem. Int. Ed.* **2005**, *44*, 6899–6901.
[22] I. Pozo, Z. Huang, F. Lombardi, D. Alexandropoulos, F. Kong, M. Slota, J.-R. Deng, W. Stawski, P. Horton, S. Coles, *ChemRxiv.* **2023**, https://doi.org/10.26434/chemrxiv-2022-1v5b4-v2.
[23] D. Ranieri, F. Santanni, A. Privitera, A. Albino, E. Salvadori, M. Chiesa, F. Totti, L. Sorace, R. Sessoli, *Chem. Sci.* **2023**, *14*, 61–69.
[24] C. J. Kingsbury, M. O. Senge, *Coord. Chem. Rev.* **2021**, *431*, 213760.
[25] R. D. McCurdy, P. H. Jacobse, I. Piskun, G. C. Veber, D. J. Rizzo, R. Zuzak, Z. Mutlu, J. Bokor, M. F. Crommie, F. R. Fischer, *J. Am. Chem. Soc.* **2021**, *143*, 4174–4178.
[26] A. Ryan, A. Gehrold, R. Perusitti, M. Pintea, M. Fazekas, O. B. Locos, F. Blaikie, M. O. Senge, *Eur. J. Org. Chem.* **2011**, 5817–5844.
[27] N. Aratani, A. Osuka, *Org. Lett.* **2001**, *3*, 4213–4216.
[28] T. Tanaka, B. S. Lee, N. Aratani, M. C. Yoon, D. Kim, A. Osuka, *Chem. Eur. J.* **2011**, *17*, 14400–14412.
[29] T. Yamabayashi, M. Atzori, L. Tesi, G. Cosquer, F. Santanni, M.-E. Boulon, E. Morra, S. Benci, R. Torre, M. Chiesa, L. Sorace, R. Sessoli, M. Yamashita, *J. Am. Chem. Soc.* **2018**, *140*, 12090–12101.
[30] R. K. Al-Shewiki, M. Korb, A. Hildebrandt, S. Zahn, S. Naumov, R. Buschbeck, T. Rüffer, H. Lang, *Dalton Trans.* **2019**, *48*, 1578–1585.
[31] L. A. Fendt, H. Fang, M. E. Plonska-Brzezinska, S. Zhang, F. Cheng, C. Braun, L. Echegoyen, F. Diederich, *Eur. J. Org. Chem.* **2007**, 4659–4673.

[32] R. W. Boyle, C. K. Johnson, D. Dolphin, *J. Chem. Soc. Chem. Commun.* **1995**, 527–528.
[33] N. Miyaura, K. Yamada, A. Suzuki, *Tetrahedron Lett.* **1979**, *20*, 3437–3440.
[34] J. M. O'Brien, E. Sitte, K. J. Flanagan, H. Ku, L. J. Hallen, M. O. Senge, *J. Org. Chem.* **2019**, *84*, 6158–6173.
[35] S. Horn, B. Cundell, M. O. Senge, *Tetrahedron Lett.* **2009**, *50*, 2562–2565.
[36] Deposition numbers 2257145 (for **1**), 2260447 (for **2**), 2257146 (for **6**), and 2257147 (for **8**) contain the supplementary crystallographic data for this paper. These data are provided free of charge by the joint Cambridge Crystallographic Data Centre and Fachinformationszentrum Karlsruhe Access Structures service.
[37] S. Stoll, A. Schweiger, *J. Magn. Reson.* **2006**, *178*, 42–55.
[38] C. Finazzo, C. Calle, S. Stoll, S. Van Doorslaer, A. Schweiger, *Phys. Chem. Chem. Phys.* **2006**, *8*, 1942–1953.
[39] A. Wolberg, J. Manassen, *J. Am. Chem. Soc.* **1970**, *92*, 2982–2991.
[40] A. Bencini, D. Gatteschi, *Electron Paramagnetic Resonance of Exchange Coupled Systems*, Springer, Berlin, **1990**.
[41] A. Osuka, S. Nakajami, T. Nagata, K. Maruyama, K. Torium, *Angew. Chem. Int. Ed. Engl.* **1991**, *30*, 582–584.
[42] C. J. Kingsbury, K. J. Flanagan, H. G. Eckhardt, M. Kielmann, M. O. Senge, *Molecules* **2020**, *25*, 3195.
[43] S. Takahashi, J. Van Tol, C. C. Beedle, D. N. Hendrickson, L. C. Brunel, M. S. Sherwin, *Phys. Rev. Lett.* **2009**, *102*, 087603.
[44] G. R. Eaton, S. S. Eaton, in *Distance Measurements in Biological Systems by EPR* (Eds.: L. J. Berliner, G. R. Eaton, S. S. Eaton), Kluwer Academic/Plenum Publishers, New York, **2000**, pp. 29–154.
[45] M. Atzori, L. Tesi, E. Morra, M. Chiesa, L. Sorace, R. Sessoli, *J. Am. Chem. Soc.* **2016**, *138*, 2154–2157.
[46] J. L. Du, G. R. Eaton, S. S. Eaton, *J. Magn. Reson. Ser. A* **1996**, *119*, 240–246.
[47] F. Santanni, A. Albino, M. Atzori, D. Ranieri, E. Salvadori, M. Chiesa, A. Lunghi, A. Bencini, L. Sorace, F. Totti, R. Sessoli, *Inorg. Chem.* **2021**, *60*, 140–151.
[48] M. Warner, S. Din, I. S. Tupitsyn, G. W. Morley, A. M. Stoneham, J. A. Gardener, Z. Wu, A. J. Fisher, S. Heutz, C. W. M. Kay, G. Aeppli, *Nature* **2013**, *503*, 504–508.
[49] I. Borilovic, P. J. Alonso, O. Roubeau, G. Aromí, *Chem. Commun.* **2020**, *56*, 3139–3142.
[50] M. Atzori, S. Benci, E. Morra, L. Tesi, M. Chiesa, R. Torre, L. Sorace, R. Sessoli, *Inorg. Chem.* **2018**, *57*, 731–740.
[51] O. Kahn, Y. Journaux, I. Morgenstern-Badarau, J. Galy, J. Jaud, *J. Am. Chem. Soc.* **1982**, *104*, 2165–2176.
[52] S. Hiroto, A. Osuka, *J. Org. Chem.* **2005**, *70*, 4054–4058.
[53] B. J. Littler, M. A. Miller, C. H. Hung, R. W. Wagner, D. F. O'Shea, P. D. Boyle, J. S. Lindsey, *J. Org. Chem.* **1999**, *64*, 1391–1396.
[54] J. S. Lindsey, H. C. Hsu, I. C. Schreiman, *Tetrahedron Lett.* **1986**, *27*, 4969–4970.
[55] F. Neese, *Wiley Interdiscip. Rev.: Comput. Mol. Sci.* **2018**, *8*, e1327.
[56] A. D. Becke, *J. Chem. Phys.* **1993**, *98*, 5648–5652.
[57] C. Lee, W. Yang, R. G. Parr, *Phys. Rev. B* **1988**, *37*, 785.
[58] S. Grimme, S. Ehrlich, L. Goerigk, *J. Comput. Chem.* **2011**, *32*, 1456–1465.
[59] S. Grimme, J. Antony, S. Ehrlich, H. Krieg, *J. Chem. Phys.* **2010**, *132*, 154104–154123.
[60] L. Noodleman, J. G. Norman, *J. Chem. Phys.* **1979**, *70*, 4903–4906.
[61] A. Bencini, F. Totti, *J. Chem. Theory Comput.* **2009**, *5*, 144–154.
[62] C. Adamo, V. Barone, A. Bencini, F. Totti, I. Ciofini, *Inorg. Chem.* **1999**, *38*, 1996–2004.
[63] T. Hasobe, K. Ida, H. Sakai, K. Ohkubo, S. Fukuzumi, *Chem. Eur. J.* **2015**, *21*, 11196–11205.
[64] T. Morotti, M. Pizzotti, R. Ugo, S. Quici, M. Bruschi, P. Mussini, S. Righetto, *Eur. J. Inorg. Chem.* **2006**, *2006*, 1743–1757.
[65] M. A. Bakar, N. N. Sergeeva, T. Juillard, M. O. Senge, *Organometallics* **2011**, *30*, 3225–3228.
[66] G. R. Fulmer, A. J. M. Miller, N. H. Sherden, H. E. Gottlieb, A. Nudelman, B. M. Stoltz, J. E. Bercaw, K. I. Goldberg, *Organometallics* **2010**, *29*, 2176–2179.
[67] O. V. Dolomanov, L. J. Bourhis, R. J. Gildea, J. A. K. Howard, H. Puschmann, *J. Appl. Crystallogr.* **2009**, *42*, 339–341.
[68] G. M. Sheldrick, *Acta Crystallogr. Sect. A* **2015**, *71*, 3–8.
[69] C. F. MacRae, I. Sovago, S. J. Cottrell, P. T. A. Galek, P. McCabe, E. Pidcock, M. Platings, G. P. Shields, J. S. Stevens, M. Towler, P. A. Wood, *J. Appl. Crystallogr.* **2020**, *53*, 226–235.
[70] E. Zolotoyabko, *J. Appl. Crystallogr.* **2009**, *42*, 513–518.

Manuscript received: September 1, 2023
Accepted manuscript online: October 9, 2023
Version of record online: October 23, 2023